



# Dynamic Analysis of the Rock Burst Potential of a Longwall Panel Intersecting with a Fault

Lishuai Jiang<sup>1,2</sup> · Peng Kong<sup>1</sup> · Peipeng Zhang<sup>1</sup> · Jiaming Shu<sup>1</sup> · Qingbiao Wang<sup>1</sup> · Lianjun Chen<sup>1</sup> · Quanlin Wu<sup>3</sup>

Received: 14 February 2019 / Accepted: 21 October 2019 / Published online: 16 November 2019  
© Springer-Verlag GmbH Austria, part of Springer Nature 2019

## Abstract

Faults are one of the most common geological structures in underground mining. Affected by mining activities, fault-slip events will release large amounts of energy and trigger seismic waves, which could induce rock burst events and endanger mining operations. In this study, a longwall panel intersecting with a fault is introduced, as well as field microseismic (MS) monitoring. Static and dynamic numerical analyses are conducted to investigate the fault parameters' effects on the behaviors of the fault. The results show that the friction angle ( $\varphi_f$ ) significantly affects the shear displacement, magnitude and distribution of the seismic moment; the fault stiffness has a great effect on the magnitude of the seismic moment but smaller effects on the shear displacement and the distribution of the seismic moments. Based on the influence of the fault stiffness and  $\varphi_f$  on the seismic moment, reasonable fault parameters can be determined. By employing the calibrated parameters, the dynamic responses and the rock burst potential of the surrounding rocks were analyzed by means of the peak particle velocity (PPV) and stress distribution. The propagation of the seismic waves released by fault-slip events excites the particle velocity of the rock mass, and there is a strong correlation between the particle velocity and rock mass damage. As the working face advances toward the fault, the PPV and stress fluctuation of the peak abutment stress rise significantly, which result in a great increase in the rock burst potential. The rock burst potential changes with the mining activities; therefore, corresponding measures must be applied to prevent and control rock burst events. This study contributes to deepening our understanding of the fault parameters in numerical simulations and the dynamic responses and rock burst potential of the surrounding rocks due to mining activities and provides a back-analysis calibration method for the fault parameters.

**Keywords** Rock burst potential · Fault-slip · Seismic moment · Peak particle velocity · Stress distribution

## List of Symbols

$L$	Distance of the working face from the fault
$H$	Distance of the fault from the coal seam roof
$M_0$	Seismic moment
$G$	Shear stiffness
$A$	Area of the fault where shear slip occurs
$D$	Shear displacement
$M_c$	Cumulative seismic moment

$E_i$	Elastic modulus
$\nu$	Poisson's ratio
$c$	Cohesion
$\sigma_t$	Tensile strength
$\varphi_f$	Friction angle
$F_{smax}$	Maximum shear force
$F_s$	Shear force
$c_{if}$	Contact surface cohesion
$A_i$	Area represented by the contact surface node
$F_n$	Normal force
$\mu$	Pore pressure
PPV	Peak particle velocity
$\sigma_p$	Peak abutment stress

✉ Peng Kong  
17854859770@163.com

<sup>1</sup> State Key Laboratory of Mining Disaster Prevention and Control, Shandong University of Science and Technology, Qingdao 266590, China

<sup>2</sup> State Key Laboratory for Geomechanics and Deep Underground Engineering, China University of Mining and Technology, Beijing 100083, China

<sup>3</sup> Department of Chemistry and Chemical Engineering, Jining University, Qufu 273100, Shandong, China

## 1 Introduction

A rock burst is one of the most hazardous issues encountered during underground mining. This phenomenon always involves a violent release of energy, with a large rock deformation and rock ejection that can cause severe damage to openings and equipment and may result in fatalities (Wang et al. 2006; Hosseini 2017; Mazaira and Konicek 2015; Li et al. 2016a, b; Zhang et al. 2017). With the ever-increasing mining depths, coal mines in China, Poland, the United States, etc., have begun to suffer from the threat of rock bursts. There are more than 170 coal mines in China that have a rock burst potential, and more than 4000 rock burst accidents have occurred, resulting in hundreds of casualties and more than 30 km of roadway damage (Wang et al. 2019).

Rock bursts are generally characterized into three types, namely, strain burst, pillar burst, and fault-slip burst, depending on the volume of the rock masses involved and the underlying mechanism by which the rock bursts are induced (Ortlepp and Stacey 1994; Blake and Hedley 2004). A critically stressed fault can slip when the shear stresses reach the shear strength, particularly when the degrees of freedom are changed when it is intersected by a mine opening or by the yield zone surrounding a mining area. Ortlepp and Stacey (1994) noted that compared with the other two types of rock bursts, fault-slip burst releases more energy, with the  $M_L$  (Richter or local magnitude) of the associated seismic events ranging from 2.5 to 5.0. Therefore, among the three types of rock bursts, fault-slip bursts are likely to cause the most damage to large rock mass areas. The source of the seismic events may even be located far from the burst sites (Hedley 1992; Ortlepp and Stacey 1994).

Practice and studies have shown that the vicinage of faults will greatly increase the rock burst potential. In the Witwatersrand gold deposit in South Africa, many rock

burst accidents with huge energies have occurred under the influence of faults (Stewart et al. 2001). Among the 50 rock burst accidents that occurred in the Longfeng Coal Mine, 72% were related to faults, and 62% occurred when roadways were close to the faults (Kong et al. 2019). Influenced by the F16 reverse fault, a working face of the Yuejin Coal Mine in China suffered several rock burst accidents during mining, which could have had severe safety impacts on the mining operation. Figure 1 shows the roadway deformation and damage caused by one of the Yuejin Coal Mine rock bursts (Li et al. 2016b).

Physical tests and analyses are strong methods for evaluating the rock burst potential of rocks. However, analyzing the rock burst potential of a field case requires the consideration of multiple geological and geotechnical conditions, such as the ground stress distribution, mechanical properties of the rock strata and faults, excavation range of the panel, etc. Numerical simulations are thus also a useful tool. Ji et al. (2012) and Wu (2017) studied the rock burst potential near a fault under different mining sequence conditions using FLAC3D, a finite difference software (Itasca 2009). Their studies show that a reasonable mining sequence can effectively reduce the rock burst potential. Jiang et al. (2017) and Manouchehrian and Cai (2018) studied the influence of the dip angle and length of a fault on rock burst events, and their research showed that the rock burst potential increases with the fault dip and length. Numerical simulation is capable of conducting a dynamic analysis on a large scale, making it surely useful for analyzing the rock burst potential of underground openings near a fault (Bizzarri 2012; Sainoki and Mitri 2014a, b; Wang and Cai 2017).

It is well accepted that fault-slip will release a large amount of energy and trigger seismic waves, which will induce a dynamic response in the surrounding rock mass of underground openings. In severe cases, the induced dynamic load may cause support failure, roof instability or even rock burst events (Blake and Hedley 2004; Alber and Fritschen 2011; Hofmann and Scheepers 2011; Zhang et al. 2019).



Fig. 1 Damage of the roadway caused by a rock burst

The characteristics of the triggered seismic waves depend on the properties and behaviors of the fault. In a numerical analysis of the rock stability under dynamic loading due to fault-slip, properly simulating the fault behavior is essential for validating the results. Sainoki and Mitri (2014a, b, 2016, 2017) conducted several studies on the seismic waves released by a fault under the influence of mining. The studies showed that the friction angle, stiffness and roughness of the fault have significant effects on the induced seismic waves. However, due to the complexity of the fault structure, the fault parameters are difficult to accurately determine, and it is often necessary to rely on empirical assumptions. The guidelines for estimating the fault parameters in numerical simulations have not been extensively discussed in the previous work. In this study, a case study of an underground coal seam that intersects a fault is introduced, as well as the microseismic (MS) monitoring of the field. A 3D model is built with FLAC3D to analyze the rock burst potential induced by fault-slip during a retreat-mining operation, and static and dynamic analyses are conducted to investigate the effects of the fault parameters on the behaviors of the fault. Upon understanding these effects, a back analysis is performed to properly calibrate the fault parameters, and the particle velocity and stress distribution are used to analyze the dynamic responses of the surrounding rocks of the retreating face. Furthermore, by analyzing the evolution of the peak abutment stress and the PPV during retreat mining, the rock burst potential caused by the existence of the intersecting fault is discussed. This study contributes to deepening our understanding of the fault parameters in numerical simulations and the dynamic responses and the rock burst potential of the surrounding rocks due to mining activities

and provides a back-analysis calibration method for the fault parameters.

## 2 Case Study

### 2.1 Geological Conditions and Rock Burst Overview in Dongtan Coal Mine

The Dongtan Coal Mine is located in Jining, Shandong Province, in the eastern part of China, as shown in Fig. 2. The fully mechanized retreating longwall mining method is employed to extract the coal seams of all panels in this mine. The mining coal seam is a coal seam with an average thickness of 8 m that is nearly horizontal and has a strong rock burst tendency. The fault structure in the minefield is developed and has a significant influence on the roadway layout and safe production.

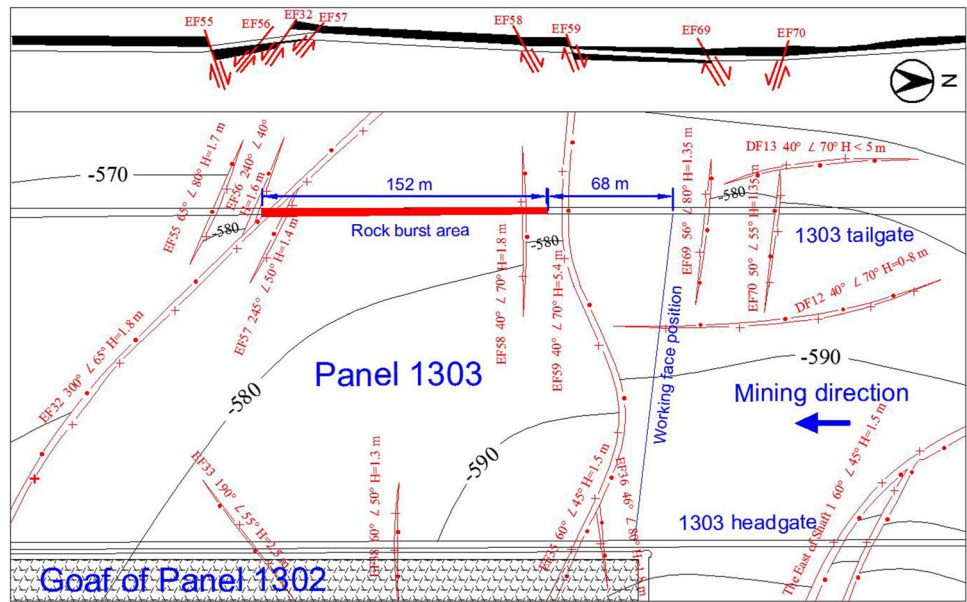
A fault-related rock burst event happened in panel 1303 of Dongtan Coal Mine. The coal seam depth of panel 1303 is approximately 580 m, and the average thickness of the coal seam is 8 m. Panel 1303's faults are very densely distributed, so the panel has to pass through faults for recovery. When panel 1303 is mined to the vicinity of the EF59 fault, a serious rock burst accident occurs, causing the severe deformation of the tailgate from 68 to 220 m in front of the working face. The layout of panel 1303 and rock burst accident occurrence position are shown in Fig. 3. According to the seismic station monitoring, the magnitude of the rock burst accident reached 1.9, and it occurred between two fault groups. The two fault groups cut the coal rock formation and caused the stratum between the faults to rise significantly,

**Fig. 2** Location map of the Dongtan Coal Mine





**Fig. 3** Layout of panel 1303 in the Dongtan Coal Mine



forming a barrier structure. The coal with a strong rock burst tendency and the hard roof rock layer provide conditions for accumulating a large amount of energy in the coal rock mass. The activation and release of the energy in the fault affected by mining is the main cause of the accident.

**2.2 Analysis of Microseismic (MS) Field Events**

The SOS MS monitoring system (developed in Poland) has been installed and applied in the Dongtan Coal Mine since the end of May 2010. The system mainly consists of a central computer, a real-time monitoring recorder server, sensors, and a digital transmission system. There are two main types of sensors: geophones and monitoring probes. The monitoring frequency range of the single sensor is 0–150 Hz, with a sensibility of  $110 \text{ Vm/s} \pm 10\%$ , sampling rate of 500 Hz, 2 bit A/D converter, response range of hundreds of meters, and minimum positioning energy of 100 J. The signal was converted into a digital signal by a digital transmission system, which transmitted the data to a real-time monitoring recorder server or central computer via a cable.

The average thickness of the coal seam of panel 14310 is 8 m, and the immediate roof is approximately 4 m of mudstone. The basic roof is mainly composed of siltstone and sandstone. A typical geological column based on core logging is shown in Fig. 4. The panel has a depth of 540 m, a width of 230 m and a strike length of 800 m, and the area around the panel is unexcavated. The panel has a complicated geological structure, in which the NF6 fault intersects panel 14310, with a dip angle of  $60^\circ$  and drop of 6–10 m. The panel is mined through the fault from the footwall, and the layout of the panel is shown in Fig. 5.

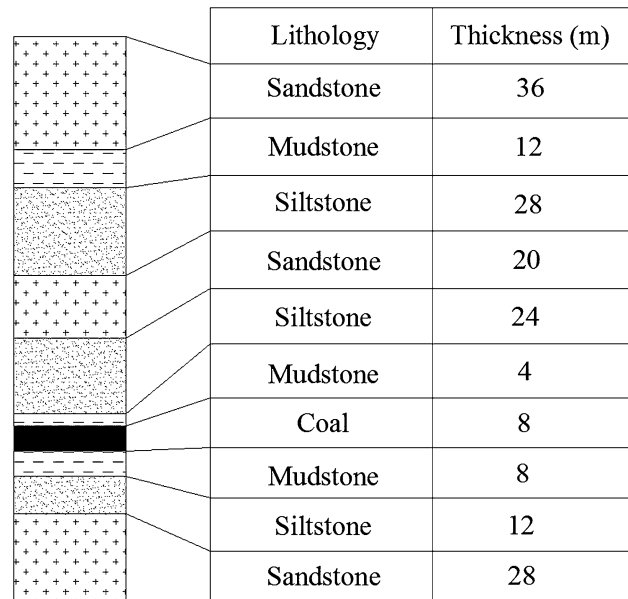


**Fig. 4** Typical geological column

Figure 6 shows the distribution of MS events during the period of mining the panel through the NF6 fault.  $L$  represents the distance from the fault of the working face. When  $L$  is positive, it means that the working face is at the footwall; when  $L$  is negative, it means that the working face is at the hanging wall.  $H$  represents the distance from the coal seam roof of the fault. When  $H$  is positive, it means that the fault is above the coal seam roof; when  $H$  is negative, it means that the fault is below the coal seam roof. Figure 6a shows the distribution of MS events for  $50 \text{ m} < L \leq 100 \text{ m}$ . The MS events mainly occurred in the roof rock strata at  $H < 65 \text{ m}$

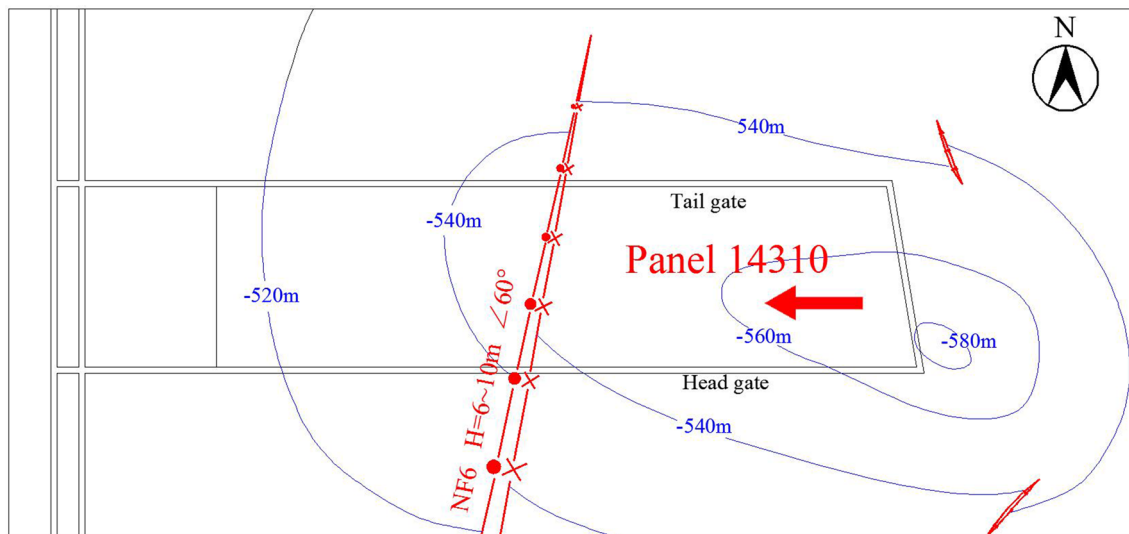


**Fig. 5** Layout of panel 14310 in the Dongtan Coal Mine

with a sporadic distribution. The recorded maximum-energy MS event occurred in the sandstone, which is 40 m above the coal seam; the energy of this MS was 5.4e3 J. Figure 6b shows the distribution of MS events when  $0 \text{ m} \leq L \leq 50 \text{ m}$ . During this period, the frequency and energy level of the MS events obviously increased, the MS events were mainly concentrated in the vicinity of the fault, and the height of the strata where the MS events occurred was higher into the roof at 100 m above the coal seam. When  $L = 20 \text{ m}$  and  $L = 0 \text{ m}$ , two major MS events with energies greater than  $1\text{e}4 \text{ J}$  occurred. Studies have shown that when the energy of an MS event is greater than  $1\text{e}4 \text{ J}$ , it can induce a rock burst (Kong et al. 2019). Figure 6c shows the distribution of MS events when  $-50 \text{ m} \leq L < 0 \text{ m}$ . At this time, the frequency and magnitude of the MS events are obviously reduced, and the height of the rock strata where the MS events occur is also obviously reduced.

Mining activities near faults cause the stress state of the fault to change, resulting in a shear slip. The seismic moment  $M_0$  released by fault-slip is related to the magnitude of the shear displacement of the fault ( $D$ ). The seismic moment  $M_0$  can indicate the magnitude of the energy released by the fault-slip (Sainoki and Mitri 2016; Domański and Gibowicz 2008). The calculation formula of  $M_0$  is as shown in Eq. (1),

$$M_0 = GAD, \quad (1)$$

where  $G$  is the shear stiffness of the fault,  $A$  is the area of the fault where the shear slip occurs, and  $D$  is the average shear displacement.

With the continuous mining of the working face, the microseismic (MS) events induced by the fault shear slip during the working face crossing the fault are counted. The

seismic moments ( $M_0$ ) of these MS events are added together to obtain the cumulative seismic moments ( $M_c$ ) under different positions of the working face. The  $M_c$  when mining the panel through the fault is shown in Fig. 7. When  $L \geq 30 \text{ m}$ ,  $M_c$  increases very slowly, which indicates that the fault is less affected by the mining. When the distance between the working face and the fault is less than 30 m,  $M_c$  increases obviously, and the extent to which the fault is affected by the mining is significantly increased. The  $M_c$  near the fault tends to be stable after the working face is mined through the fault, and there are few MS events released by the fault-slip. For a better description of the distribution of the mining-induced seismic moment in different regions along the fault when the panel is mined to the fault location, the entire fault is divided into five regions, as shown in Fig. 8a. It can be seen from Fig. 8b that the  $M_0$  released by the fault-slip is mainly concentrated at the parts of the fault in the area below 84 m of the coal seam roof (F2, F3 and F4), accounting for 84% of the cumulative seismic moment. The parts of the fault at the floor position and far from the coal seam provide only a small amount of the seismic moment (F1 and F5).

### 3 Simulation Methodology

#### 3.1 Model Establishment and Rock Mechanics Parameters

According to the geological profile of panel 14310 of the Dongtan Coal Mine, a FLAC3D numerical model is established that is 710 m long, 450 m wide and 180 m high. Considering the boundary effect, the excavation range is not less than 100 m from the model boundary, as shown in Fig. 9.

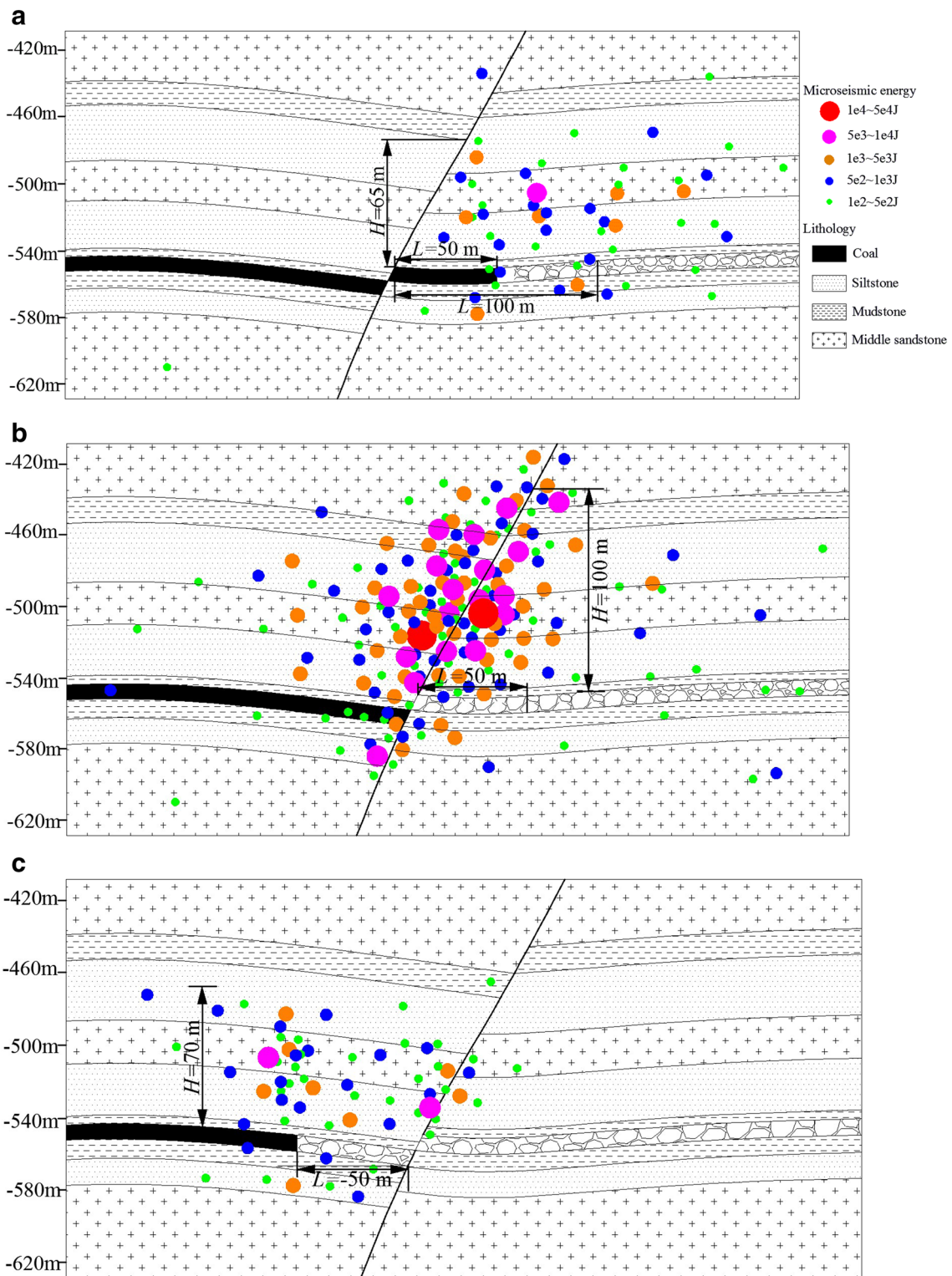


**Fig. 6** Distribution of MS events when mining the panel through a fault

The dip angle of the fault is  $60^\circ$ , the drop of the fault is 8 m, and the panel is mined through the fault from the footwall. The mechanical parameters of the rock mass are estimated

according to the complete rock properties and the generalized Hoek–Brown failure criterion. The mechanical parameters of the coal and rock mass are shown in Table 1.

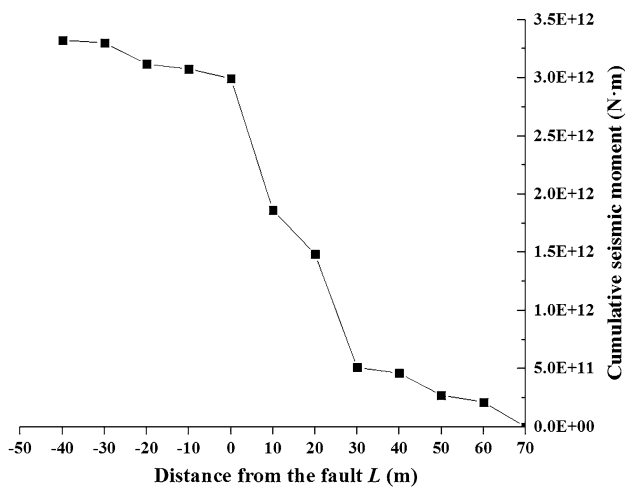


Fig. 7 Cumulative seismic moment ( $M_c$ ) when mining the working face through the fault

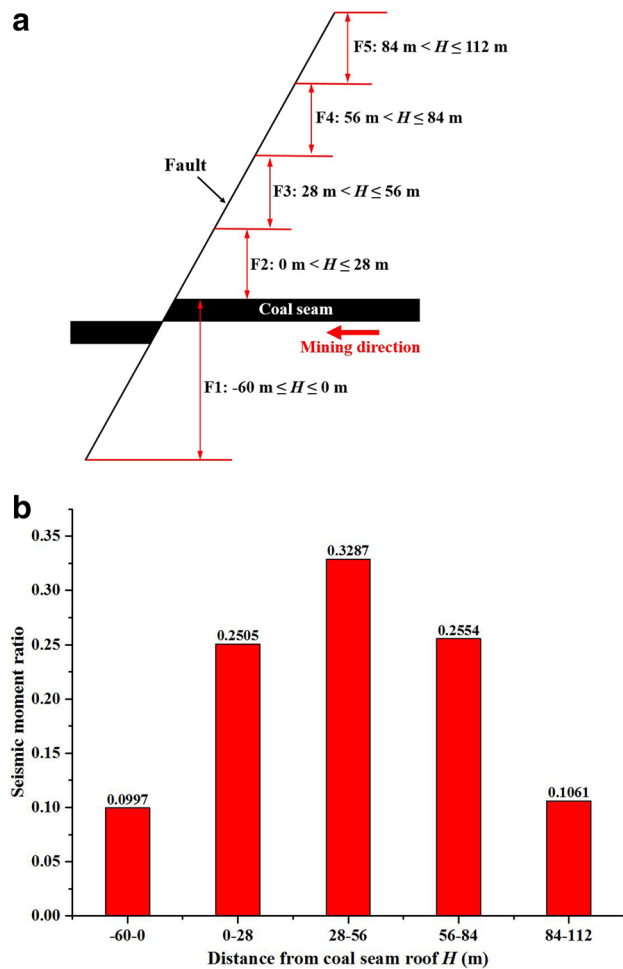


Fig. 8 Field-measured seismic moment distribution characteristics. **a** Five regions of the fault. **b** Field-measured distribution of the seismic moments ( $M_0$ )

No displacement in the direction perpendicular to the side boundaries is allowed. The depth of the simulated coal seam is 540 m. A vertical stress of 10.8 MPa is applied at the top boundary of the model to simulate the overburden pressure by assuming that the overlying unit weight is 0.025 MN/m<sup>3</sup> with the force of gravity applied (Jiang et al. 2019a, b). In situ stresses are applied in the form of an initial stress with the horizontal-to-vertical stress ratios set to 0.6 and 0.8 in the x- and y-directions, respectively, according to the in situ stress measurement.

### 3.2 Simulation of the Fault Behavior

The fault is simulated using the interface contact surface command. The contact surface is an element with no thickness, and the constitutive model is a Coulomb shear model. For the Coulomb sliding contact surface elements there are two states: intact and broken. According to the Coulomb shear strength criterion, the shear force  $F_{smax}$  required for the relative sliding of the contact surface can be obtained as (Itasca 2009):

$$F_{smax} = c_{if}A + \tan \varphi_f (F_n - \mu A), \tag{2}$$

where  $c_{if}$  is the contact surface cohesion;  $A$  is the area represented by the contact surface node;  $\varphi_f$  is the friction angle of the contact surface node;  $F_n$  is the normal force, and  $\mu$  is the pore pressure.

When the shear force on the contact surface is smaller than the maximum shear force ( $|F_s| < F_{smax}$ ), the contact surface is in the elastic stage. When the shear force on the contact surface equals the maximum shear force ( $|F_s| = F_{smax}$ ), the contact surface enters the plastic stage.

Although many laboratory tests have been conducted on the mechanical properties of faults, the scale effects are still unclear due to the limitations of laboratory specimens (Sainoki and Mitri 2014b; Li et al. 2019; Feng et al. 2019a, b). It is commonly recognized that fault zones have a low stiffness due to the cracks and fractures produced by past shear movements, but the degree to which the stiffness of a rockmass within fault zones decreases is dependent upon a number of factors, due to the complex internal structure of the fault and various factors such as fault filling and weathering. In most cases, the cohesion and tensile strength of the fault are very small, so they are set to 0. (Sainoki and Mitri 2014a). Therefore, this paper focuses on the study of the fault shear stiffness, normal stiffness and friction angle ( $\varphi_f$ ).

### 3.3 Dynamic Analysis Procedures

Dynamic research on the law of the fault activity during the continuous retreat mining of a panel is conducted. In each mining cycle, 10 m of the panel is mined along its



Fig. 9 Numerical model

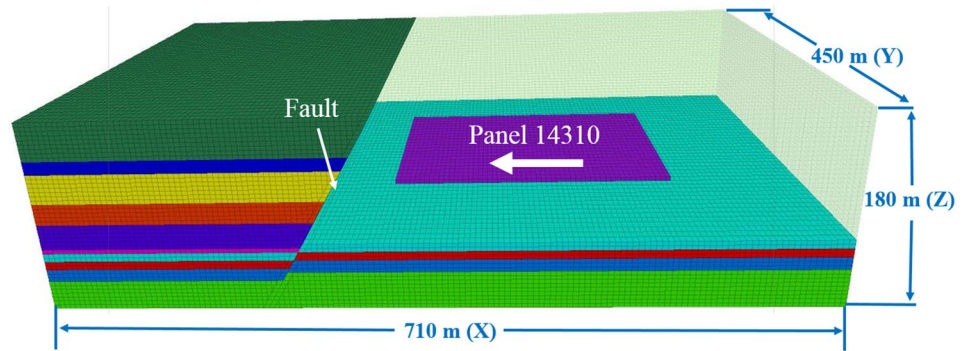


Table 1 Rock mass properties

Lithology	$E_i$ (GPa)	$\nu$	$c$ (MPa)	$\sigma_t$ (MPa)	$\varphi_f$ (°)
Middle sandstone	10.5	0.22	3	0.62	34.5
Siltstone	6.7	0.24	2.1	0.37	31
Mudstone	2.9	0.28	1.2	0.2	29
Coal	1.1	0.34	0.9	0.12	26

$E_i$  is the elastic modulus,  $\nu$  is Poisson’s ratio,  $c$  is cohesion,  $\sigma_t$  is tensile strength,  $\varphi_f$  is the friction angle

strike under static analysis conditions, and then either the dynamic analysis is triggered or the next mining cycle is simulated, depending on whether the Coulomb shear strength criterion is met, that is, the shear stress of the fault reaches the shear strength. The numerical calculation process is shown in Fig. 10. Static analyses were performed to simulate the mining activities and the induced stress distribution. The mining-induced effects on the fault-slip (i.e., the fault stress and the shear displacement of the fault) are evaluated after the static analysis. If the shear displacement of the fault ( $D$ ) is smaller than 0.01 m, the seismic moment released by the fault-slip is negligible, so the seismic parameter  $M_0$  for the dynamic analysis is calculated in the region where  $D > 0.01$  m (Sainoki and Mitri 2014a, b). The dynamic analysis method can simulate the influence of the fault-slip on underground openings, so it can more accurately evaluate the rock burst potential influenced by the fault.

During the static analysis, the model boundary is fixed in the direction perpendicular to the boundary plane. For a dynamic analysis to simulate the fault-slip in the source region, the boundary conditions are changed to viscous in order to prevent the model boundaries from reflecting the seismic waves arising from the fault-slip. The viscous boundary condition is based on the use of independent dashpots (mechanical viscous dampers) in the normal and shear directions at the model boundaries in order to effectively absorb the energy of the seismic waves, particularly when

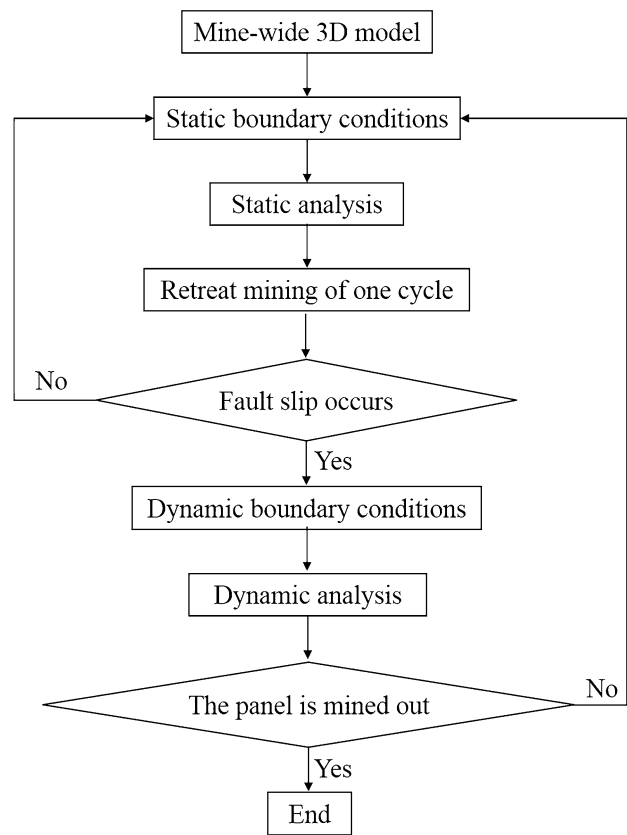


Fig. 10 Flowchart of the dynamic analysis

the angles of incidence are greater than 30° (Itasca 2009). The seismic source is simulated in the form of a concentrated force. The waveform of the seismic wave is a half sine wave, the frequency is 25 Hz, and the vibration time is one cycle. Local damping is chosen as the damping form. The damping ratio for rock falls between 2 and 5%. Thus, 5% of the critical damping is adopted for this study (Sainoki and Mitri 2017; ABAQUS 2003).



### 4 Analysis and Determination of Fault Parameters

In the numerical analysis of faults, the proper simulation of the fault behavior is obviously one of the most important factors for ensuring the validity of the simulation results. In this section, the effects of the fault parameters (friction angle and stiffness) on the fault behaviors are investigated, and a back analysis method based on field microseismic monitoring data for the purpose of estimating the proper parameters is introduced.

#### 4.1 Effect of Fault Parameters on the Shear Displacements of the Fault

Figure 11a and Table 2 show the shear displacements ( $D$ ) at different heights along the fault with respect to the fault friction angle ( $\varphi_f$ ) when the working face has been mined to the fault ( $L=0$ ). The monitoring line is arranged on the fault at  $y=225$  m. Note that the monitoring points at different heights along the fault are marked with  $H$ , the maximum shear displacement of each scenario is marked with  $D_{max}$  and the area where  $D$  is greater than 90% of  $D_{max}$  is recognized with a large shear displacement area and marked with red in Fig. 11a. The  $\varphi_f$  of the fault has a significant effect on the fault-slip behavior, and  $D$  and  $D_{max}$  show negative correlations with  $\varphi_f$ . In the case of  $\varphi_f=30^\circ$ , a large shear displacement occurs 24–40 m above the coal seam roofline ( $24\text{ m} \leq H \leq 40\text{ m}$ ), and  $D_{max}$  is 0.29 m. When the fault position is 80 m above the coal seam, there is almost no slip and it remains stable. When  $\varphi_f$  is decreased to  $15^\circ$ ,  $D_{max}$  increases dramatically to 0.66 m, and the area with a

**Table 2** Effect of the friction angle ( $\varphi_f$ ) on the shear displacement of the fault ( $D$ )

$\varphi_f$ ( $^\circ$ )	$D_{max}$ (m)/ $H$ (m)	Area with large shear displacement (m)
15	0.66/56	$36 \leq H \leq 76$
20	0.53/48	$32 \leq H \leq 64$
25	0.42/36	$28 \leq H \leq 52$
30	0.29/32	$24 \leq H \leq 40$

large shear displacement extends higher to  $36\text{ m} \leq H \leq 76\text{ m}$ . The shear displacement of the entire fault is considerably increased with the reduction of  $\varphi_f$ .

It is commonly recognized that faults have a low stiffness due to the cracks and fractures produced by past shear movements, but the degree to which the stiffness of the rock mass within the faults decreases is dependent upon a number of factors. Therefore, the fault stiffness parameter is very difficult to determine (Sainoki and Mitri 2017). As mentioned by Ivins and Lyzenga (1986), the fractures and cracks within faults could decrease the shear modulus of the rock mass by up to one-fifteenth. According to the study on the dynamic behavior of mining-induced fault-slips by Sainoki and Mitri (2014b & 2017), the shear and normal stiffnesses of the fault do not have a significant influence on the fault shear displacement under the assumption that the shear and normal stiffnesses of the fault are 10%, 20% or 30% of the shear modulus of the surrounding rock mass. It can be seen from the distribution of MS events presented in Sect. 2.2 that the MS events primarily occurred in the siltstone region. Therefore, to investigate their effect on the shear displacement, the shear stiffness and normal stiffnesses of the fault are set as

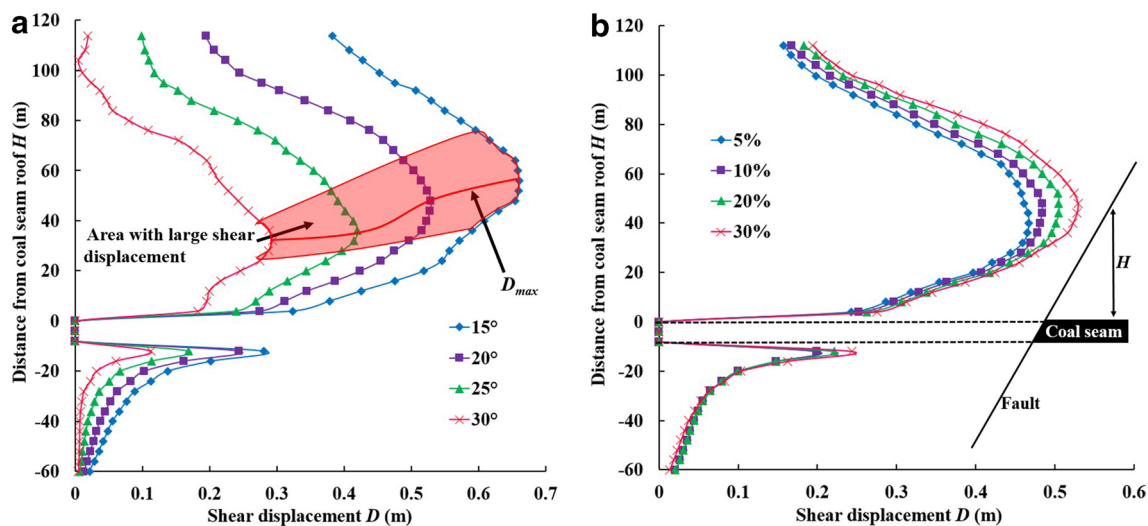


**Fig. 11** Effect of the fault parameters on the shear displacement of the fault. **a** Friction angle ( $\varphi_f$ ). **b** Shear stiffness and normal stiffness

**Table 3** The shear stiffness and normal stiffness of the fault

Fault-to-rock stiffness ratio (%)	Shear stiffness (GPa)	Normal stiffness (GPa)
5	0.14	0.34
10	0.27	0.67
20	0.54	1.34
30	0.81	2.01

5%, 10%, 20% and 30% of the stiffness of the siltstone, as shown in Table 3.

Figure 11b shows the effect of the stiffness of the fault on the shear displacement when  $L=0$  m, and it can be seen that the stiffness is positively correlated to  $D$ .  $D_{\max}=0.53$  m in the case where the fault-to-rock stiffness ratio is equal to 30%, and then it is slightly reduced to 0.47 m as the ratio is reduced to 5%. Although the stiffness's effect on the shear displacement is not significant, an overall change in  $D$  from  $H > 20$  m of the fault can be observed with the change in the stiffness.

From the above analysis, it is known that  $D$  is mainly affected by the friction angle of the fault, essentially unaffected by the stiffness, and shows a negative correlation with  $\varphi_f$ .

### 4.2 Effect of Fault Parameters on the Seismic Moment

The seismic moment ( $M_0$ ) can be calculated from Eq. (3), which is obtained by summarizing the seismic moments ( $M_0$ ) of each structural plane element  $i$ . As the panel continues to be mined, the  $M_0$  values in the process of mining the panel through the fault are accumulated to obtain the cumulative seismic moment ( $M_c$ ). Figure 12 shows the cumulative seismic moment ( $M_c$ ) along the entire fault and its spatial distribution with respect to the fault friction angle ( $\varphi_f$ ).

$$M_0 = GAD = G \sum a_i d_i \tag{3}$$

Figure 12a shows the evolution of  $M_c$  with retreat mining starting at  $L=60$  m and passing the fault at  $L=-40$  m. Note that  $M_c$  is the cumulative seismic moment along the entire fault, which describes the magnitude of the mining-induced seismicity. As seen, the friction angle ( $\varphi_f$ ) of the fault has a significant influence on  $M_c$  in the following two aspects: (1)  $M_c$  is inversely proportional to  $\varphi_f$ , and the maximum  $M_c$  in the case  $\varphi_f=15^\circ$  is  $3.9 \times 10^{12}$  N m, which is more than four times the value when  $\varphi_f=30^\circ$  and (2) a fault with a low  $\varphi_f$  will be more susceptible to mining, as  $M_c$  can be detected when the face is still far from the fault. In the case of  $\varphi_f=15^\circ$ , the reading of  $M_c$  begins at  $L=50$  m. As  $\varphi_f$

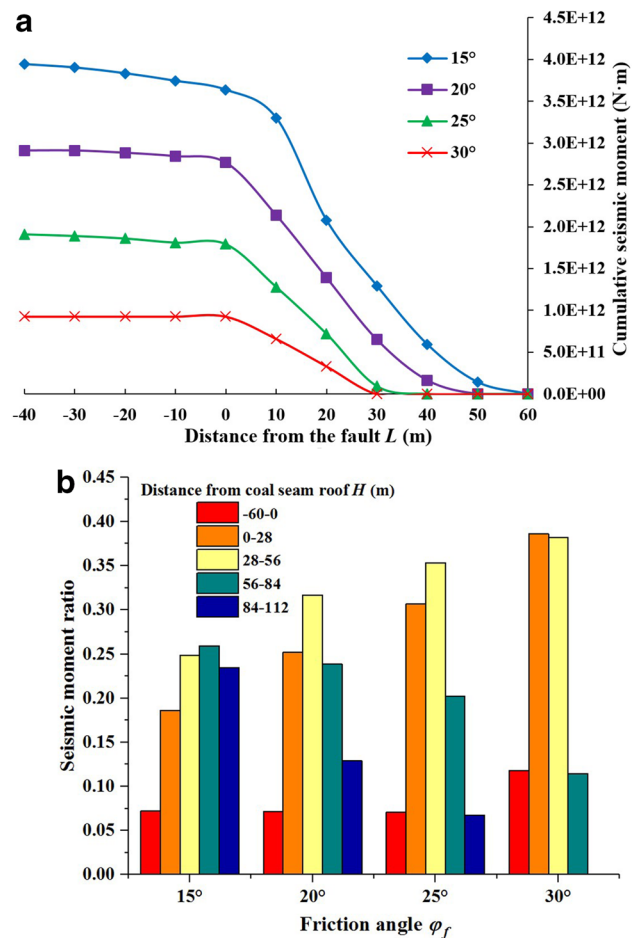


**Fig. 12** Effect of the friction angle on the cumulative seismic moment and the distribution of the seismic moments. **a** Cumulative seismic moment ( $M_c$ ). **b** Distribution of the seismic moments ( $M_0$ )

increases to  $30^\circ$ , the initiation of the seismicity is delayed to  $L=30$  m.

Figure 12b and Table 4 show the distribution pattern of  $M_0$  occurring along the fault with respect to  $\varphi_f$ . It can be seen that in addition to the magnitude of  $M_c$ ,  $\varphi_f$  also greatly affects the distribution pattern of the seismic moment ( $M_0$ ) along the fault. In the case of  $\varphi_f=15^\circ$ , 74.2% of  $M_0$  occurs in

**Table 4** Effect of the friction angle on the spatial distribution of the seismic moments

Regions of the fault	Seismic moment ratio $M_0/M_c$ (%)			
	$\varphi_f=15^\circ$	$\varphi_f=20^\circ$	$\varphi_f=25^\circ$	$\varphi_f=30^\circ$
F1 ( $-60 \text{ m} \leq H \leq 0 \text{ m}$ )	7.2	7.2	7.1	11.8
F2: ( $0 \text{ m} \leq H \leq 28 \text{ m}$ )	18.6	25.2	30.7	38.6
F3: ( $28 \text{ m} \leq H \leq 56 \text{ m}$ )	24.9	31.7	35.3	38.2
F4: ( $56 \text{ m} \leq H \leq 84 \text{ m}$ )	25.9	23.9	20.2	11.4
F5: ( $84 \text{ m} \leq H \leq 112 \text{ m}$ )	23.4	12.9	6.7	0

the regions of  $F_3$ ,  $F_4$  and  $F_5$ , and approximately one-fourth of the  $M_0$  is in each region. Such results indicate that the fault-slip behavior at the fault in the high roof has a more active response to mining, thereby causing a high magnitude of  $M_0$ . With the increase in  $\varphi_f$ , the  $M_0$  that occurs at  $F_5$  is dramatically decreased and is completely eliminated when  $\varphi_f$  reaches  $30^\circ$ , and the same tendency can be found for  $M_0$  in  $F_4$ . In the meantime,  $M_0$  in  $F_2$  and  $F_3$  increases significantly with  $\varphi_f$ . When  $\varphi_f = 15^\circ$ , 18.6% and 24.9% of the total  $M_0$  occurred in  $F_2$  and  $F_3$ , respectively, and the numbers reach 38.6% and 38.2% as  $\varphi_f$  increases to  $30^\circ$ , with most of the  $M_0$  concentrated within  $0 \text{ m} \leq H \leq 56 \text{ m}$  of the fault. The fault in the coal seam and the floor is less sensitive to mining, as  $M_0$  in  $F_1$  is unnoticeably changed.

According to Fig. 11, the shear displacements of the fault significantly decrease with an increase in  $\varphi_f$ , especially in the high roof area ( $F_5$ ). As is known from Eq. (1),  $M_0$  is positively correlated with  $D$ , which explains the decrease of  $M_0$  in  $F_5$  with an increasing  $\varphi_f$ .

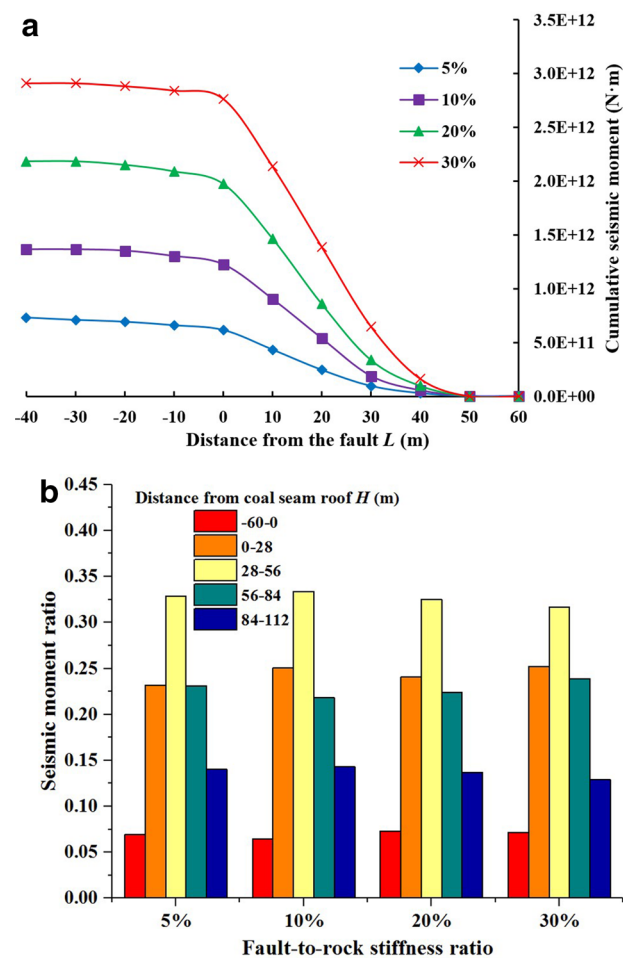


Fig. 13 Effect of the fault stiffness on the cumulative seismic moment and the distribution of the seismic moments. **a** Cumulative seismic moment ( $M_c$ ). **b** Distribution of the seismic moments

Figure 13 shows the cumulative seismic moment ( $M_c$ ) of the fault and its distribution pattern of  $M_0$  with respect to the stiffness of the fault. The stiffness of the fault greatly affects the fault’s behavior in a positive correlation manner in terms of the slip-induced seismic moment. Taking the  $M_c$  data at  $L=0$  as an example, when the fault-to-rock stiffness ratio decreases from 30 to 5%,  $M_c$  increases from  $6.2 \times 10^{11}$  to  $2.8 \times 10^{12}$  N m. Different from the effect of  $\varphi_f$ , the stiffness of the fault only affects  $M_c$  in terms of its magnitude; the sensitivity of the fault to mining does not change because the starting point and increased tendency of  $M_c$  show no relevance to the ratio. Additionally, Fig. 13b shows no notable effect of the fault stiffness on the distribution pattern of the seismic moment.

In summary, the friction angle significantly affects the shear displacement, magnitude and distribution of the seismic moment. Because the strength of the faults is a function of the normal stress, the friction coefficient of the fault surface, its waviness and dilation characteristics, etc. (Kaiser and Cai 2012), these results indicate that when a fault is smooth with fewer asperities, a thicker filling or a higher weathering degree, the fault will be low in  $\varphi_f$ , which makes it more sensitive to mining-induced stress, and it tends to slip in shear. If fault-slip occurs, more intense seismicity will be induced (Barton and Choubey 1977; Barton 1973; Meng et al. 2018). The results agree with those of the previous study by Sainoki (2014b). The fault stiffness has a great effect on the magnitude of the seismic moment but less of an effect on the shear displacement and the distribution of seismic moments.

Therefore, for a numerical analysis based on a specific case, it is better to calibrate the fault parameters instead of using a simple assumption. Otherwise, the simulation of the fault behaviors is difficult to verify. In the following section, a back analysis method based on MS monitoring is introduced to determine the proper fault parameters.

### 4.3 Determination of the Fault Parameters Based on Back Analysis

According to the previous sections, the fault-slip behaviors due to mining activities, i.e., the shear displacements and the seismic moments, are affected by the fault parameters ( $\varphi_f$  and the stiffness), although the effect varies. It can be concluded that the fault parameters are fundamental to describing the mechanical behaviors of the fault-slip in numerical modeling. Therefore, it is essential to calibrate the fault parameters before the numerical analysis to ensure its validity. Because it is quite challenging to measure the shear displacement of a fault on-site (Wang et al. 2017), the  $M_0$  released by the fault-slip can be obtained by MS monitoring (as introduced in Sect. 2.2). Therefore, the  $M_0$  based on field monitoring can be employed as a practical indicator in the back analysis or calibration of the fault parameters.

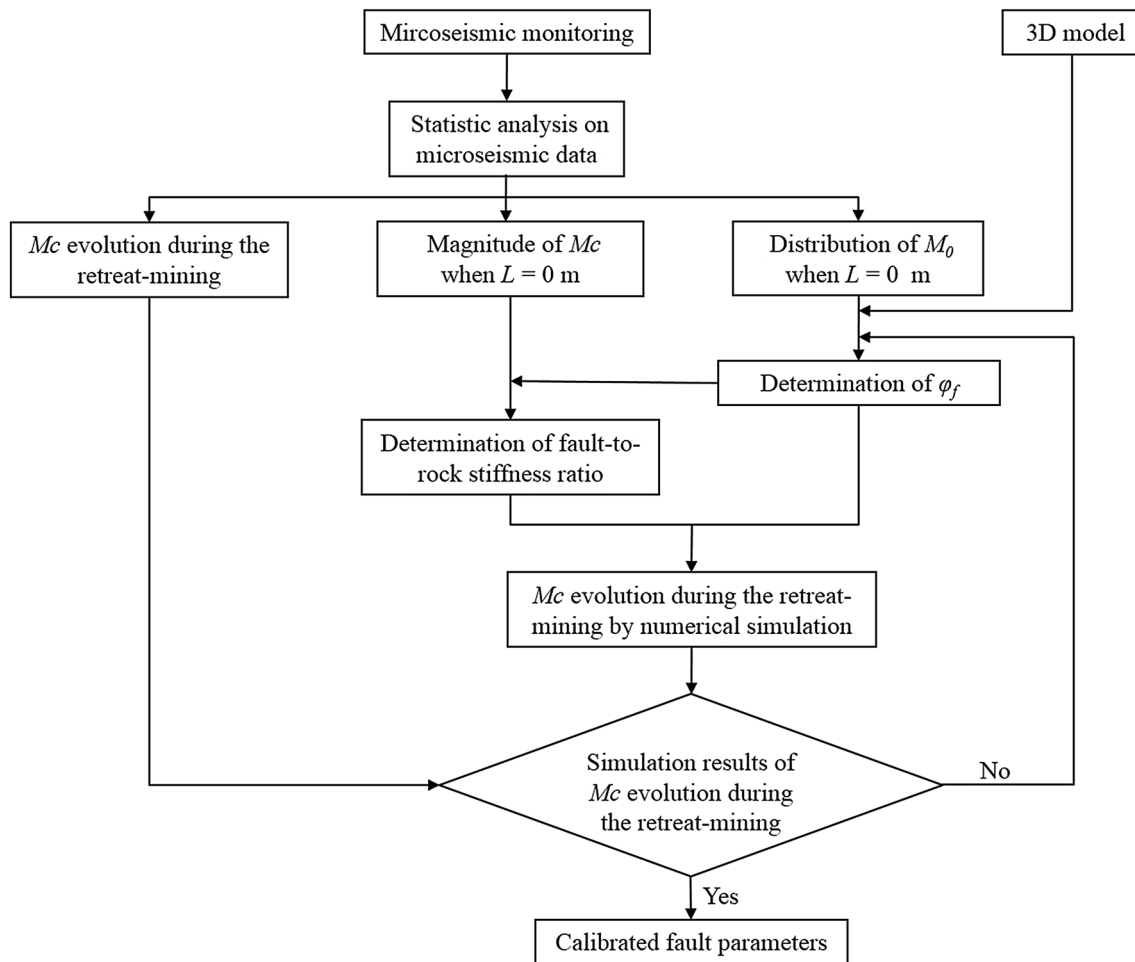


Fig. 14 Flowchart of the back analysis of the fault parameters

In this study, a trial-and-error back analysis is conducted to determine  $\varphi_f$  and the stiffness of the fault by comparing  $M_c$  and the distribution of  $M_0$  in the simulations to those obtained from field monitoring, with a flow chart of the back analysis shown in Fig. 14. First, MS monitoring data of the panel should be collected and statistically analyzed, and a mine-wide 3D model should be built according to the geological and geotechnical information of the panel. According to Sect. 4.2, the distribution of the seismic moment is a distinguishing and effective parameter for back-analyzing  $\varphi_f$ , so  $\varphi_f$  can be preliminarily determined by trial-and-error simulations with different  $\varphi_f$  by comparing the distribution pattern of  $M_0$  to that of the field monitoring when  $L=0$  m. Figure 15a shows a comparison of the spatial distribution of  $M_0$  for different  $\varphi_f$  and the spatial distribution of  $M_0$  for field monitoring. Through an analysis of variance, when  $\varphi_f$  is  $20^\circ$ , the squared coefficient of correlation is the highest, 0.92. Then, the fault stiffness can be determined by  $M_c$  at  $L=0$  m. After the preliminary determination, a calibration analysis with the preliminarily determined parameters is required. If the  $M_c$  evolution during the retreat

mining from the numerical analysis shows good agreement with the field monitoring data, the employed fault parameters could be recognized as a set of valid parameters. Figure 15b shows the evolution of  $M_c$  with different stiffnesses when the  $\varphi_f$  of the fault is  $20^\circ$  and the evolution of  $M_c$  is monitored in the field. Through an analysis of variance, when the  $\varphi_f$  of the fault and the ratio of the stiffness of the faulted rock mass are  $20^\circ$  and 30%, respectively, the squared coefficient of correlation is 0.98. Therefore, the numerical simulation results are in good agreement with the field monitoring results.

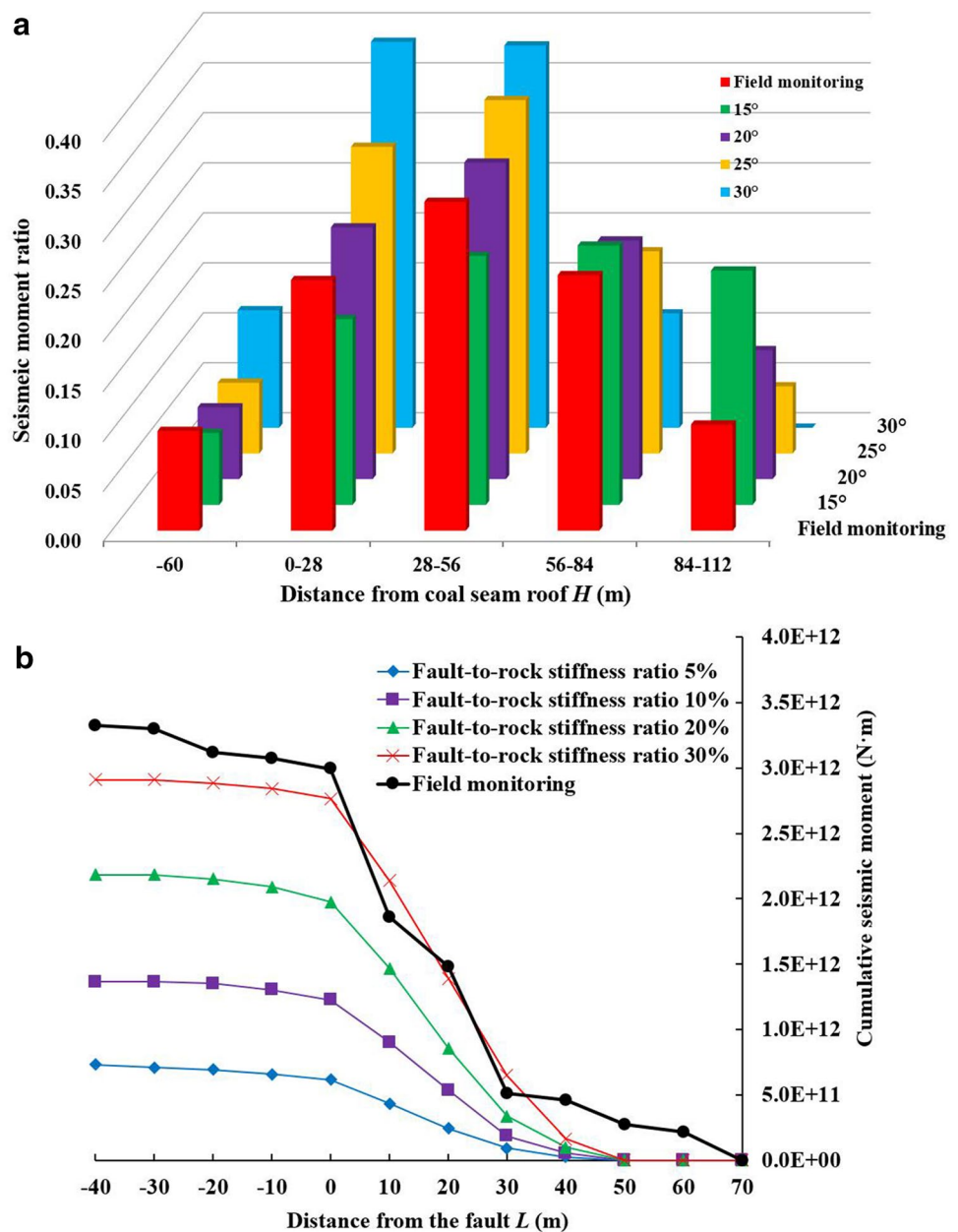
## 5 Analysis of the Dynamic Response Due to a Mining-Induced Fault-Slip

### 5.1 The Particle Velocity Evolution over the Mining Operation

The propagation of seismic waves excites the particle velocity of the rockmass, and there is a strong correlation between



**Fig. 15** Comparison of numerical simulation results and field-measured results. **a** Distribution of the seismic moments ( $M_0$ ). **b** Cumulative seismic moment ( $M_c$ )



the particle velocity and rockmass damage (Brinkmann 1987; Hedley 1992; Weng et al. 2017; Wu et al. 2019). Strong mining seismic events are the source of the very high values of the peak particle velocity (PPV) recorded in the near-wave field. The high value of the PPV can exert a high dynamic load on the support and underground excavation. As a result of the significant increase in the dynamic load, rock burst phenomena are observed in the excavations. Mutke et al. (2009, 2015) conducted a statistical analysis of 120 rock burst events in the Upper Silesian Coal Basin from 1988 to 2006. 90% of the rock bursts took place after those tremors that produced a peak particle velocity (PPV) with a value from 0.05 to 1.0 m/s, and the distance between the inducing tremor

and the damaged areas did not exceed 100 m. An empirical criterion for the potential rock burst hazard has been developed based on a database of rock bursts.

- (a) Lack of hazard:  $PPV \leq 0.05$  m/s.
- (b) Low hazard:  $0.05 < PPV \leq 0.2$  m/s.
- (c) Medium hazard:  $0.2 < PPV \leq 0.4$  m/s.
- (d) High hazard:  $PPV > 0.4$  m/s.

It should be emphasized here that the local state of the static stresses constitutes a very important factor having an essential influence on the probability of occurrence of a rock burst as a result of the dynamic stresses caused by a mining

tremor. Local faults, the geological structure, the mining conditions, supports and remains in the referred to seam cause local areas with increased static stresses. Such places are much more prone to rock bursts at relatively small values of PPV. Thus, the particle velocity due to the fault-slip is an important indicator for evaluating the induced seismic waves in the dynamic analysis (Sainoki and Mitri 2014a, 2016).

Figure 14 shows the particle velocity distribution after the seismic waves are triggered by fault-slip when the working face is 40 m, 20 m, 10 m and -20 m from the fault ( $L=40$  m, 20 m, 10 m and -20 m, respectively), and no fault-slip is detected when  $L>40$  m. According to Fig. 16, when  $L=40$  m, the fault-slip only occurs at a high level of the fault, and the intensity of the fault-slip is not strong because the detected particle velocity is low in both its magnitude and distribution extent. As the face advances toward the fault, almost all of the fault above the coal seam has slipped in the case of  $L=20$  m. The seismic moments released are significantly increased, resulting in a significant increase in the vibration velocity of the rock mass near the fault above the coal seam. The fault-slip continuously

extends to the seam and the floor when  $L=10$  m, and seismic waves with a high particle velocity can be observed surrounding the working face. Under such circumstances, the working face may experience severe dynamic loading and have a great potential of dynamic hazards (e.g., rock burst). After the working face has mined past the fault, the particle velocity significantly decreases, as well as the distribution.

The longwall mining operation induces a series of intensive stratum movements and stress readjustments (Peng 2008). The high concentrated stress ahead of the working face is often referred to as the peak abutment stress ( $\sigma_p$ ), which is a paramount parameter for the operation planning and support design.  $\sigma_p$  is usually located tens of meters ahead of the face. With its inherent high stress, the coal under  $\sigma_p$  would be more sensitive to seismic waves than coal elsewhere. Under the impact of a certain seismic wave, coal with a high stress may fail in a violent manner and eject to the working face, resulting in rock burst hazards and endangering personnel and machinery. In this section, the peak particle velocity (PPV) at point  $\sigma_p$  is recorded with the retreat mining, as illustrated in Fig. 17.

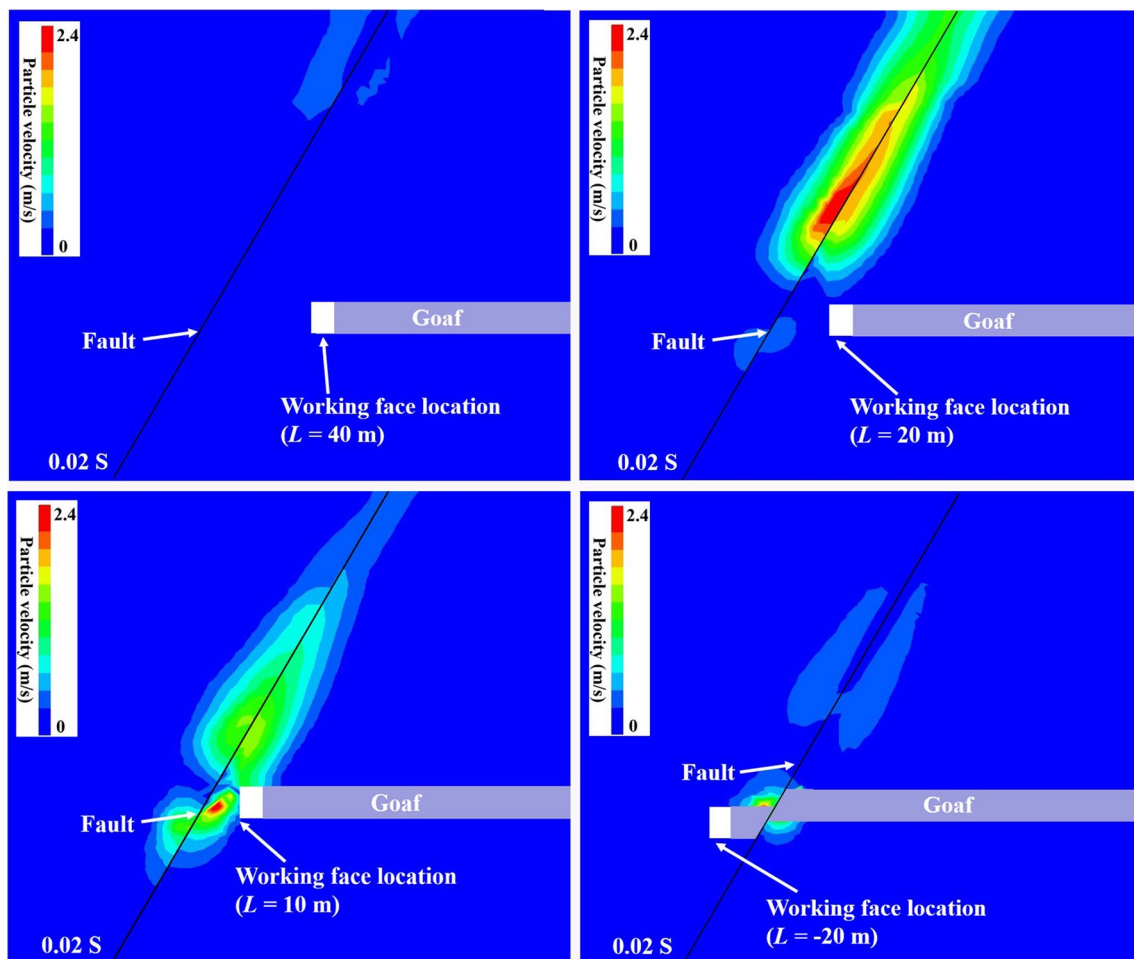


Fig. 16 The distribution of the particle velocity with respect to the retreat-mining of the working face

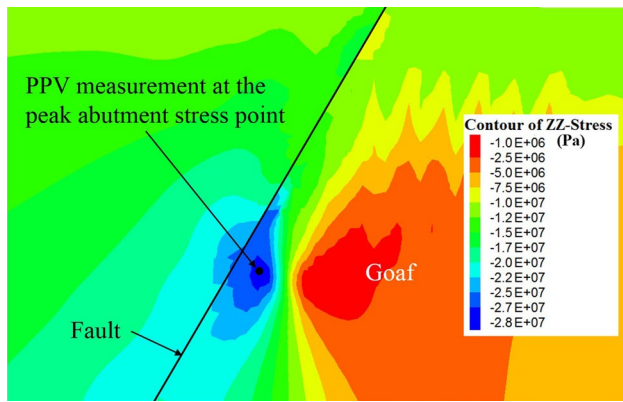


Fig. 17 PPV measurement at the peak abutment stress point

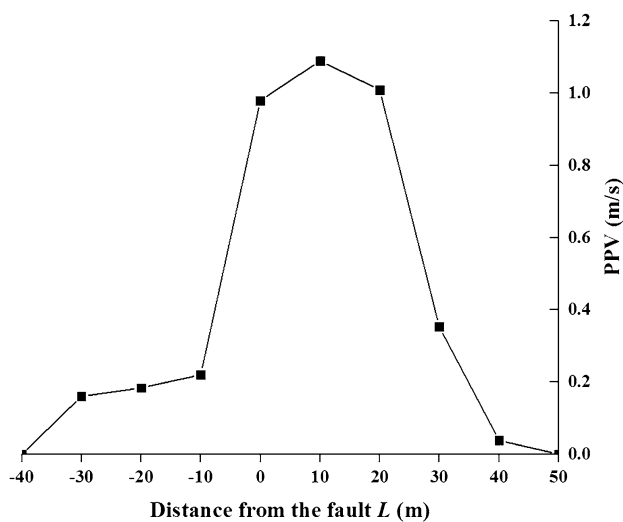


Fig. 18 PPV evolution with retreat mining

The recorded PPV evolution with the retreat mining is shown in Fig. 18. As seen, the PPV at point  $\sigma_p$  is minor before the working face reaches 40 m from the fault ( $L \geq 40$  m). The PPV first increases exponentially to 1.01 m/s when  $40 \text{ m} \geq L \geq 20$  m and then gradually reaches its peak (1.09 m/s) at  $L = 10$  m. The PPV begins to decrease after the working face is less than 10 m from the fault and then sharply decreases to 0.22 m/s after the face has been mined through the fault. According to Brinkmann (1987), a PPV of approximately 1 m/s is sufficient to induce a rock burst, resulting in a severe deformation of the roadway or rock fall. When the working face is mined through the fault, the PPV is less than 0.22 m/s, a significant reduction. By analyzing the PPV when the working face is at different positions, it can be seen that the PPV is affected by the fault-slip, and the potential of a rock burst is significantly increased when the distance between the working face and the fault is less than 30 m. Monitoring and prevention measures for rock

burst hazards should therefore be strengthened under these conditions.

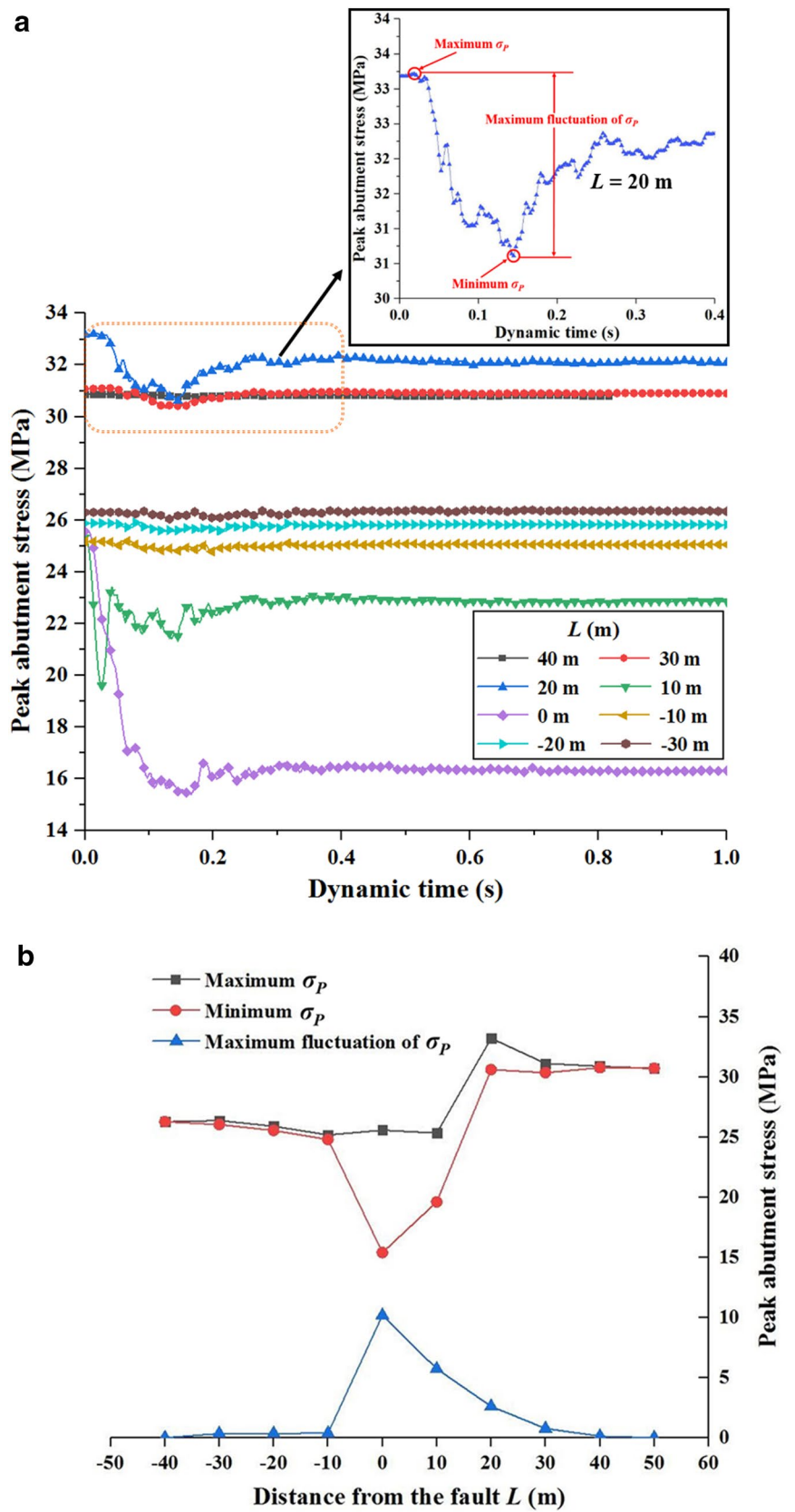
### 5.2 Evolution of the Abutment Stress with the Mining Operation

As described above, if the surrounding rock masses are in critical conditions under high stress, dynamic waves may break the original stability and trigger dynamic rock failure, e.g., rock burst. Figure 19 shows the stress fluctuation of  $\sigma_p$  after a dynamic analysis is initiated at a different phases of mining. It can be seen that the response of the stress to dynamic loads varies with  $L$ . Before  $L$  reaches 20 m, there is no noticeable stress fluctuation. However, when  $20 \text{ m} \geq L \geq 0$  m, great stress fluctuations are induced by the dynamic load. The maximum fluctuation of  $\sigma_p$  gradually increases as the face approaches the fault, with values of 2.6 MPa, 5.7 MPa and 10.6 MPa for  $L = 20$  m, 10 m, and 0 m, respectively. In all three cases,  $\sigma_p$  drops after the stress fluctuation, which indicates that the rock masses fail and can no longer sustain high stress after the dynamic load. Failures of highly stressed rock masses will release a great amount of stress and energy, which increases the rock burst potential. After the face has passed the fault, the curves of  $\sigma_p$  return to stability.

### 6 Discussion

Based on the analysis for the case of a panel intersection with a fault (presented in Sect. 5), the rock burst potential under such a circumstance could be analyzed with three parameters, i.e.,  $\sigma_p$ , PPV and the maximum fluctuation of  $\sigma_p$ , as shown in Fig. 20. When the face is far from the fault, all three parameters remain steady (class-II).  $\sigma_p$  could be high or low depending on the depth and other geological conditions. If the stress state is high, regular MS monitoring and destress measures should be taken. As the face approaches the fault, the three parameters significantly increase;  $\sigma_p$  increases due to the existence of the fault, and the mining-induced stress redistribution may initiate the fault-slip and induce seismic waves, which propagate through the rock masses as dynamic loads. As previously introduced, a high PPV indicates that the rock masses are sensitive to the dynamic load and may consequently cause a rise in the stress fluctuation. Under such circumstances, the rock burst potential can be classified as a high potential (class-I), which means that effective rock burst control measures must be applied. Generally, there are three types of rock burst prevention and control methods: (1) alternative mining methods; (2) ground preconditioning, such as destress blasting and slotting (Zhao et al. 2018; Konicek et al. 2013); and (3) rock support with a good energy-absorbing capacity (Li 2010; Mazaira and

**Fig. 19** Fluctuation of the peak abutment stress in the dynamic analysis





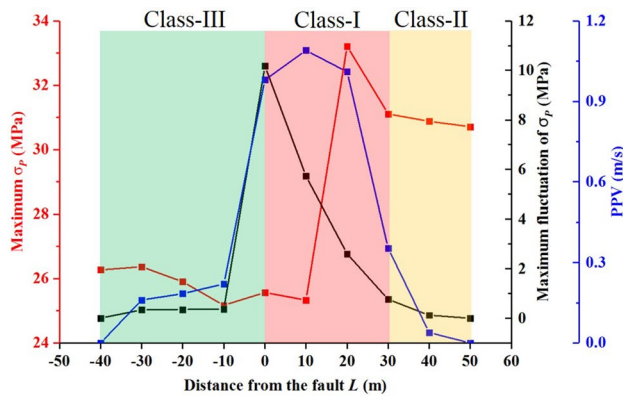


**Fig. 20** Rock burst potential with respect to the retreat-mining activities

Konicek 2015; Fu et al. 2019). For the case with a given mining method and geological conditions, proper applications of the other methods are required in areas with a high rock burst potential.

After the face has been mined past the fault, the three parameters significantly drop, among which the PPV and maximum stress fluctuation are reduced to nearly zero and the rock burst potential also becomes relatively low (class-III).

The criteria for the rock burst potential analysis under such geological conditions vary from case to case.  $L$ , the distance between the face and the fault, could be used as a practical and effective indicator for field rock burst control. The work of this study lays the foundation for studies on fault-slip burst potential analyses as future research, such as a rock burst potential identification system that may include, but is not limited to, the aforementioned parameters.

## 7 Conclusion

A case study on the rock burst potential of a longwall panel intersecting with a fault is performed. The on-site microseismic (MS) monitoring data indicates that when the working face is mined to the vicinity of the fault, the frequency and energy level of MS events are obviously increased. The MS events are mainly concentrated near the fault, and the height of the rock layer where the MS occurs is significantly increased.

A numerical model of a longwall panel intersecting with a fault is generated by means of FLAC3D software, and the influences of the fault parameters on the fault-slip behavior are analyzed. The friction angle ( $\varphi_f$ ) significantly affects the shear displacement and the magnitude and distribution of the seismic moments. The fault stiffness has a great effect on the magnitude of the seismic moment but less of an effect on the shear displacement and the distribution of the seismic moments. Based on the influences of the fault stiffness and  $\varphi_f$  on the seismic moment, reasonable fault parameters can be determined.

A dynamic numerical analysis shows that the fault-slip seismic moment has an obvious effect on the PPV and peak abutment stress ( $\sigma_p$ ) ahead of a working face that is being mined through a fault. The rock burst potential could be analyzed with  $\sigma_p$ , the PPV and the maximum fluctuation of  $\sigma_p$  to evaluate the influence of the seismic moment released by the fault-slip. As the working face approaches the fault,  $\sigma_p$ , the PPV and the maximum fluctuation of  $\sigma_p$  significantly increase and the rock burst potential significantly increases, so the coal and rock mass may be damaged from the seismic moment released by the fault-slip. After the working face has been mined past the fault, the three parameters drop significantly, with the degree of danger of a rock burst being obviously reduced. The rock burst potential changes with the mining activities, so corresponding measures must be applied to prevent and control the rock burst events. This study contributes to deepening our understanding of the fault parameters in numerical simulations and the dynamic responses and the rock burst potential of surrounding rocks due to mining activities, as well as providing a back-analysis calibration method for the fault parameters.

**Acknowledgements** The research of this study was sponsored by the National Natural Science Foundation of China (51704182, 51774194), the Natural Science Foundation of Shandong Province (ZR2017BEE050, ZR2017BEE045), the State Key Laboratory for Geomechanics and Deep Underground Engineering (SKLG-DUEK1725) and the Shandong University of Science and Technology, and the Graduate Innovation Fund of Shandong University of Science and Technology (SDKDYC190344).

## Compliance with Ethical Standards

**Conflict of Interest** The authors declare that they have no conflicts of interest.

## References

- ABAQUS (2003) ABAQUS online documentation: ver 64–1. Dassault Systemes, Paris
- Alber M, Fritschen R (2011) Rock mechanical analysis of a M1 = 4.0 seismic event induced by mining in the Saar district, Germany. *Geophys J Int* 186:359–372
- Barton N (1973) Review of a new shear-strength criterion for rock joints. *Eng Geol* 7(4):287–332
- Barton N, Choubey V (1977) The shear strength of rock joints in theory and practice. *Rock Mech* 10(1–2):1–54
- Bizzarri A (2012) Rupture speed and slip velocity: what can we learn from simulated earthquakes? *Earth Planet Sci Lett* 317:196–203
- Blake W, Hedley DGF (2004) *Rockbursts: case studies from American hard-rock mines*. Society for mining, metallurgy, and exploration, Littleton
- Brinkmann JR (1987) Separating shock wave and gas expansion breakage mechanism. In: 2nd International Symposium on Rock Fragmentation by Blasting, pp 6–15

- Domański B, Gibowicz SJ (2008) Comparison of source parameters estimated in the frequency and time domains for seismic events at the Rudna copper mine, Poland. *Acta Geophys* 56(2):324–343
- Feng F, Li XB, Rostami J et al (2019a) Numerical investigation of hard rock strength and fracturing under polyaxial compression based on Mogi-Coulomb failure criterion. *Int J Geomech* 19(4):04019005
- Feng F, Chen SJ, Li DY et al (2019b) Analysis of fractures of a hard rock specimen via unloading of central hole with different sectional shapes. *Energy Sci Eng*. <https://doi.org/10.1002/ESE3.432>
- Fu MX, Liu SW, Jia HS, He DY (2019) Experimental study of an orientation and resin-Lifting device for Improving the performance of resin-anchored roof bolts. *Rock Mech Rock Eng*. <https://doi.org/10.1007/s00603-019-01906-5>
- Hedley DGF (1992) Rockburst handbook for Ontario hard rock mines. Ontario Mining Association, North York
- Hofmann GF, Scheepers LJ (2011) Simulating fault slip areas of mining induced seismic tremors using static boundary element numerical modelling. *Min Technol* 120(1):53–64
- Hosseini N (2017) Evaluation of the rockburst potential in longwall coal mining using passive seismic velocity tomography and image subtraction technique. *J Seismol* 21:1101–1110
- Itasca (2009) FLAC3D-fast Lagrangian analysis of continua. Itasca Consulting Group Inc, Washington
- Ivins ER, Lyzenga GA (1986) Stress patterns in an interplate shear zone: an effective anisotropic model and implications for the transverse ranges, California. *Philos Trans R Soc B Biol Sci* 318(1542):285–347
- Ji HG, Ma HS, Wang JA, Zhang YH, Cao H (2012) Mining disturbance effect and mining arrangement analysis of near-fault mining in high tectonic stress region. *Saf Sci* 50(4):649–654
- Jiang LS, Wang P, Zhang PP, Zheng PQ, Xu B (2017) Numerical analysis of the effects induced by normal faults and dip angles on rock bursts. *CR Mech* 345:690–705
- Jiang LS, Kong P, Shu JM et al (2019a) Numerical analysis of support designs based on a case study of a longwall entry. *Rock Mech Rock Eng*. <https://doi.org/10.1007/s00603-018-1728-2>
- Jiang LS, Wu QS, Wu QL et al (2019b) Fracture failure analysis of hard and thick key layer and its dynamic response characteristics. *Eng Fail Anal* 98:118–130
- Kaiser PK, Cai M (2012) Design of rock support system under rockburst condition. *J Rock Mech Geotech Eng* 4(3):215–227
- Kong P, Jiang L, Shu J et al (2019) Effect of fracture heterogeneity on rock mass stability in a highly heterogeneous underground roadway. *Rock Mech Rock Eng*. <https://doi.org/10.1007/s00603-019-01887-5>
- Konicek P, Soucek K, Stas L, Singh R (2013) Long-hole distress blasting for rockburst control during deep underground coal mining. *Int J Rock Mech Min Sci* 61:141–153
- Li CC (2010) A new energy-absorbing bolt for rock support in high stress rock masses. *Int J Rock Mech Min* 47(3):396–404
- Li T, Mu ZL, Liu GJ, Du JL, Lu H (2016a) Stress spatial evolution law and rockburst danger induced by coal mining in fault zone. *Int J Min Sci Technol* 26(3):409–415
- Li ZL, Dou LM, Cai W, Wang GF, Ding YL, Kong Y (2016b) Roadway stagger layout for effective control of gob-side rock bursts in the longwall mining of a thick coal seam. *Rock Mech Rock Eng* 49(2):621–629
- Li YC, Sun SY, Tang CA (2019) Analytical prediction of the shear behaviour of rock joints with quantified waviness and unevenness through wavelet analysis. *Rock Mech Rock Eng*. <https://doi.org/10.1007/s00603-019-01817-5>
- Manouchehrian A, Cai M (2018) Numerical modeling of rockburst near fault zones in deep tunnels. *Tunn Undergr Sp Technol* 80:164–180
- Mazaira A, Konicek P (2015) Intense rockburst impacts in deep underground construction and their prevention. *Can Geotech J* 52(10):1426–1439
- Meng FZ, Louis NYW, Zhou H, Wang ZQ (2018) Comparative study on dynamic shear behavior and failure mechanism of two types of granite joint. *Eng Geol* 245:356–369
- Mutke G, Lurka A, Dubinski J (2009) Seismic monitoring and rock burst hazard assessment in deep polish coal mines-case study of rock burst on April 16, 2008 in Wujek-Slask coal mine. In: International symposium on rockburst and seismicity in mines
- Mutke G, Dubiński Józef, Lurka Adam (2015) New criteria to assess seismic and rock burst hazard in coal mines. *Arch Min Sci* 60(3):743–760
- Ortlepp WD, Stacey TR (1994) Rockburst mechanisms in tunnels and shafts. *Tunn Undergr Sp Technol* 9(1):59–65
- Peng SS (2008) Coal mine ground control, 3rd edn. Peng SS Publisher, Morgantown
- Sainoki A, Mitri HS (2014a) Dynamic modelling of fault-slip with Barton's shear strength model. *Int J Rock Mech Min* 67(67):155–163
- Sainoki A, Mitri HS (2014b) Dynamic behaviour of mining-induced fault slip. *Int J Rock Mech Min* 66(1):19–29
- Sainoki A, Mitri HS (2016) Back analysis of fault-slip in burst prone environment. *J Appl Geophys* 134:159–171
- Sainoki A, Mitri HS (2017) Influence of mining activities on the reactivation of a footwall fault. *Arab J Geosci* 10(5):99
- Stewart RA, Reimold WU, Charlesworth EG, Ortlepp WD (2001) The nature of a deformation zone and fault rock related to a recent rockburst at western deep levels gold mine, Witwatersrand basin, south africa. *Tectonophysics* 337(3–4):173–190
- Wang X, Cai M (2017) Numerical modeling of seismic wave propagation and ground motion in underground mines. *Tunn Undergr Sp Technol* 68:211–230
- Wang SY, Lam KC, Au SK, Tang CA, Zhu WC, Yang TH (2006) Analytical and numerical study on the pillar rockbursts mechanism. *Rock Mech Rock Eng* 39(5):445–467
- Wang P, Jiang L, Zheng P (2017) Application of equivalent materials to modeling fractures in the vicinity of a normal fault in the area of mining exploitation influence. *Acta Geodyn Geomater* 14(4):475–485
- Wang GF, Gong SY, Dou LM, Cai W, Yuan XY, Fan CJ (2019) Rockburst mechanism and control in coal seam with both syncline and hard strata. *Saf Sci* 115:320–328
- Weng L, Huang L, Taheri A et al (2017) Rockburst characteristics and numerical simulation based on a strain energy density index: a case study of a roadway in linglong gold mine, china. *Tunn Undergr Sp Tech* 69:223–232
- Wu QS (2017) Study on the law mining stress evolution and fault activation under the influence of normal fault. *Acta Geodyn Geomater* 14(3):357–369
- Wu QH, Chen L, Shen BT et al (2019) Experimental investigation on rockbolt performance under the tension load. *Rock Mech and Rock Eng* 52:4605–4618
- Zhang JF, Jiang FX, Yang JB, Bai WS, Zhang L (2017) Rockburst mechanism in soft coal seam within deep coal mines. *Int J Min Sci Technol* 27(3):551–556
- Zhang ZZ, Yu XY, Wu H et al (2019) Stability control for gob-side entry retaining with supercritical retained entry width in thick coal seam Longwall mining. *Energies* 12(7):1375. <https://doi.org/10.3390/en12071375>
- Zhao TB, Guo WY, Tan YL, Yin YC, Cai LS, Pan JF (2018) Case studies of rock bursts under complicated geological conditions during multi-seam mining at a depth of 800 m. *Rock Mech Rock Eng* 51:1539–1564